Article Beitr. Phys. Atmosph., June 1989, p. 99–111
0005–8173/89/02 0099–13 $ 3.00/0 Vol. 62, No. 2

Normal Mode Energetics and Error Analysis of GLA GCM Simulations with Different Horizontal Resolutions during a Winter Month

H. L. Tanaka[1,2], E. C. Kung[1] and W. E. Baker[3]

[1]Department of Atmospheric Science, University of Missouri-Columbia, Columbia, MO 65211, USA
[2]Current affiliation: Geophysical Institute, University of Alaska-Fairbanks Fairbanks, AK 99775, USA
[3]Development Division, National Meteorological Center, Washington, DC 20233, USA

(Manuscript received August 1988, in revised form February 1989)

Abstract

Comparative energetics is presented for a series of four general circulation model simulations for January 1979 conducted by the Goddard Laboratory for Atmospheres. The simulations include cases of coarse and fine horizontal model resolutions with two slightly different initial conditions. Using a three-dimensional normal mode expansion, we find that the gravity mode energy levels are significantly reduced in the higher wavenumbers and in the higher order internal vertical modes by the increase of horizontal model resolution. The prediction error of the model experiments is measured by an error norm between the two spectral expansion coefficients of the observed and simulated atmospheres. The increase of the model resolution is found to reduce the prediction error in the planetary waves (n = 1 and 2) of the barotropic component and in the synoptic waves of the baroclinic component. It is also found that the common bias in the predictions of the first internal vertical component of wavenumber 1 is related to the misrepresentation of the Pacific blocking occurring at the predictability limit of the model atmosphere.

Zusammenfassung

Energetik der Normalschwingungen und Fehleranalyse der GLA GCM Simulationen eines Wintermonats mit unterschiedlicher horizontaler Auflösung

Eine vom Goddard Laboratory for Atmospheres durchgeführte vergleichende Energiestudie einer Reihe von vier Januarsimulationen des Jahres 1979 mit Modellen der allgemeinen Zirkulation wird vorgestellt. Die Simulationen umfassen Fälle grober und feiner horizontaler Auflösung unter zwei geringfügig verschiedenen Anfangsbedingungen. Durch Entwicklung nach dreidimensionalen Normalschwingungen finden wir, bei Vergrößerung der horizontalen Modellauflösung, daß die Schwerewellenenergie für die höheren Wellenzahlen und für die internen vertikalen Schwingungen höherer Ordnung bedeutend kleiner wird. Der Vorhersagefehler der Modellversuche wird durch eine Fehlernorm zwischen den beiden spektralen Entwicklungskoeffizienten der beobachteten und nachgebildeten Atmosphäre gemessen. Es stellt sich heraus, daß die Erhöhung der Modellauflösung den Vorhersagefehler in den planetaren Wellen (n = 1 und 2) der barotropen Komponente und in den synoptischen Wellen der baroklinen Komponente verringert. Ebenfalls zeigt sich, daß der systematische Fehler in den Vorhersagen der ersten vertikalen Komponente der Wellenzahl 1 mit der verzerrten Darstellung des an der Vorhersagbarkeitsgrenze der Modellatmosphäre auftretenden ‚Pazifik-Blockings' zusammenhängt.

1 Introduction

One of the primary objectives of the First GARP (Global Atmospheric Research Program) Global Experiment (FGGE) was to improve extended-range weather prediction models. Through the analysis of the FGGE observations and parallel simulations by the Goddard Laboratory for Atmospheres (GLA) general circulation model (GCM), Kung and Baker (1986a) have shown that the energy processes in the short-wave range of the simulations are much more intense than those in the observations for the FGGE winter. This is caused by the gain of kinetic energy in the short-wave range from the source of the synoptic-scale range through the nonlinear wave-wave interaction. The failure of the simulation to amplify ultralong waves and produce a pronounced blocking is attributed to the lack of kinetic energy input by the wave-wave interaction to ultralong waves because of the excessive down-scale cascade. By means of a three-dimensional normal mode decomposition of atmospheric energetics variables, Tanaka et al. (1986)

have shown that the above-mentioned kinetic energy transformation is accompained by the energy flow from baroclinic to barotropic components of atmospheric motion. The normal mode energetics have a specific advantage in separating energetics characteristics into Rossby and gravity modes. Tanaka et al. have reported a large reduction of high frequency gravity mode in the simulated atmosphere compared to the FGGE observation.

Based on the analysis results, four numerical simulations of January 1979 are conducted to investigate the energetics effects of grid resolutions and initial datasets. The four simulations include those of two different grid resolutions, each with two different initial datasets. Both the standard 4° x 5° latitude-longitude GLA GCM and fine resolution 2° x 2.5° GLA GCM are integrated for a one-month period using the 0000 GMT 1 January 1979 initial datasets during the FGGE as analyzed by the GLA and the Geophysical Fluid Dynamics Laboratory (GFDL).

The computational effects of increased horizontal resolution were extensively investigated by many researchers (e.g., Manabe et al., 1970; Wellck et al., 1971; Miyakoda et al., 1971; Puri and Bourke, 1974). Manabe et al. (1970) compared the results of coarse (about 500 km grid size) and fine (about 250 km) resolution models and showed that the spectral distribution of eddy kinetic energy becomes closer to that of the observed atmosphere in the fine resolution model partly due to the shift of energy dissipation toward a smaller scale. Wellck et al. (1971) compared the simulated energy spectra for 10°, 5°, and 2.5° grid models in longitude and latitude to show a noticeable improvement of the long wave spectrum at wavenumbers 1 to 4 in the 2.5° grid model. Puri and Bourke (1974) investigated the effect of a truncation on energy and enstrophy spectra in barotropic spectrals models and showed that the unrealistic energy accumulation at short waves in a coarse resolution model is released in a fine resolution model. The increase in the model resolution resulted in a reduction in short wave energy.

The effect of slightly different initial data on predictive skill was documented by Charney et al. (1986), Smagorinsky (1969), Williamson and Kasahara (1971), and Lorenz (1982) in the context of atmospheric predictability. Unavoidable initial error grows rapidly as the time integration proceeds. The predictions by the identical twin models, starting from the slightly different initial data, level off with each other to indicate that the determinstic atmospheric predictability is of the order of two weeks. The error growth is induced essentially by a nonlinear cascade of error energy from small to large scales. Yee and Shapiro (1981) and Straus (1988), on the other hand, proposed that numerical errors can be amplified as a part of the dynamics of a physically unstable system in the atmosphere. Recently, Miyakoda et al. (1986) conducted a series of one-month forecasts using three different initial conditions. They showed that the circulation patterns starting from these three initial conditions tend to be similar to each other on a one-month time scale, indicating some recognizable skill in the last ten days of the month. They suggested that extended-range forecast errors are largely due to the systematic bias which is known as climatic drift. Their study indicates a possibility of extended-range forecasting by investigating the mechanism of error growth of our dynamical-statistical forecasting models.

The effect of the increased horizontal resolution and the effect of the different initial conditions upon the climatic drift are examined in this study using a recently developed normal mode energetics scheme (see Tanaka, 1985; Tanaka et al., 1986; Tanaka and Kung, 1988). The scheme allows the diagnosis of not only the three-dimensional spectral distributions of energy and energy transformations but also the examination of the energetics characteristics of Rossby waves, gravity waves, barotropic components, and baroclinic components of the atmospheric general circulation. Prediction errors in previous studies have been assessed using conventional specific fields such as the root-mean-square error of 500 mb height or sea-level pressure (e.g., Shukla, 1985). In the normal mode expansion method, it is possible to evaluate the prediction errors for barotropic and baroclinic components or Rossby and gravity modes, using global atmospheric data. The examination of error energy spectra of predictions in terms of the normal mode expansion should provide meaningful information in order to improve the forecasting skill of the model. The characteristics of error energy spectra are presented in the present study for the wavenumber and vertical index domain with a barotropic-baroclinic decomposition.

2 Simulation Experiments and Datasets

As listed in Table 1, four simulation experiments (Exps-1, 2, 3 and 4) were conducted for the period 1–31 January 1979 with the GLA standard and high resolution GCMs. The GLA and GFDL gridded analyses of the FGGE at 0000 GMT 1 January were used as the initial data (see Daley et al., 1985; Kung and Baker, 1986a). The mean January climatology of the sea surface temperature was used in all four simulations.

The standard coarse resolution version of the GLA GMC used in the simulation is the fourth-order global

Table 1 Four simulation experiments of the January 1979 global atmosphere with GLA GCMs

Experiment	1/1/79 0000 GMT (initial data)	GCM grid size (latitude × longitude)
Exp-1	GLA	4° × 5°
Exp-2	GFDL	4° × 5°
Exp-3	GLA	2° × 2.5°
Exp-4	GFDL	2° × 2.5°

atmospheric model described by Kalnay-Rivas et al. (1977) and Kalnay et al. (1983). There are nine vertical layers equal in sigma with a uniform nonstaggered horizontal grid of 4° latitude by 5° longitude. The model is based on an energy conserving scheme in which all horizontal differences are computed with fourth-order accuracy. A 16th-order Shapiro (1970) filter is applied every two hours on the sea-level pressure, potential temperature, and wind fields. In this scheme, wavelengths longer than four grid lengths are resolved accurately without damping. Wavelengths shorter than four grid lengths, which would otherwise be grossly misrepresented by the finite differences, are filtered out while they are still infinitesimal. The energy spectrum of high-frequency gravity modes is controlled by the Matsuno (Euler-backward) time integration scheme. Poleward of 60°N the time tendency of the full model fields are filtered for unstable zonal wavenumbers as determined by a Matsuno time scheme, the fourth order spatial differencing, and a 7.5 min time step (see Takacs and Balgovind, 1983).

The 2° latitude by 2.5° longitude high resolution version of the GLA GCM is identical to the coarse resolution version with respect to the physical parameterizations. The time step of the hydrodynamics is 3.75 minutes in the high resolution version compared to 7.5 minutes in the coarse resolution version. An 8th-order Shapiro (1970) filter is used rather the 16th-order filter in coarse resolution model.

The four simulation datasets analyzed in this study include twice-daily grid-point values of geopotential height, temperature, humidity, horizontal wind and vertical velocity at 1000, 850, 700, 500, 400, 300, 250, 200, 150, 100, 70, and 50 mb at 0000 and 1200 GMT. The FGGE analysis data by the GFDL are utilized in this study to represent the observed atmosphere for evaluating the prediction errors in the simulations.

3 Scheme of Analysis

The analysis scheme of normal mode energetics is based on Tanaka (1985) and Tanaka and Kung (1988). Total energy $E = K + P$ (the sum of kinetic energy and available potential energy) for a component of three-dimensional normal mode expansion may be written as

$$E_{nlm} = \frac{1}{2} p_s h_m |w_{nlm}|^2, \tag{1}$$

where w_{nlm} is a dimensionless complex expansion coefficient of dependent variables u, v, ϕ. The dimensional factors of surface pressure of the basic state p_s and equivalent height h_m are multiplied to $|w_{nlm}|^2$ so that the energy is expressed in units of Jm^{-2}. The triple subscripts are the wavenumber n, meridional index l, and vertical index m, respectively.

The vertical modes $m = 0$ and $m \neq 0$ are regarded respectively as the barotropic (external) and baroclinic (internal) modes. Figure 1 illustrates the first six vertical structure functions as the expansion basis in the vertical (after Tanaka et al., 1986). Total energy pertaining to $m = 0$ is defined as barotropic energy and that for $m \neq 0$ baroclinic energy. There are 12 vertical analysis levels to generate the vertical modes of $m = 0$–11. A construction of vertical structure functions for very small equivalent height, particularly for $m = 11$, is extremely difficult and contains a large extent of uncertainty. For this reason, the maximum vertical index utilized in this study is $m = 10$. Global atmospheric field of each vertical index is then projected onto orthonormal Hough functions which have been computed from Laplace's tidal equation for a motionless basic state. A total of 50 meridional indicies are used, including 26 Rossby modes, and 12 eastward and 12 westward gravity modes. These meridional modes retrieve a sufficient amount of atmospheric energy of large scale motions as demonstrated in Tanaka (1985). The zonal wavenumbers $n = 0$–15 are examined in this study. Unrealistic reduction of short waves was analyzed for the coarse resolution model output beyond $n = 18$. The reduction may be explained by the Shapiro filter which filters out the wavelengths shorter than 4 grid lengths (i.e., 20° longitude). The definition of energy in (1) involves a contribution from vertical geopotential flux across the lower boundary; however, this contribution is negligibly small.

The spectral energy balance equation for a component of normal mode expansion may be written as

$$\frac{dE_{nlm}}{dt} = B_{nlm} + C_{nlm} + D_{nlm}, \tag{2}$$

where B_{nlm} is the nonlinear interaction of kinetic energy, C_{nlm} that of available potential energy, and D_{nlm} the combined energy source and sink by the diabatic processes, including dissipation. The spectral

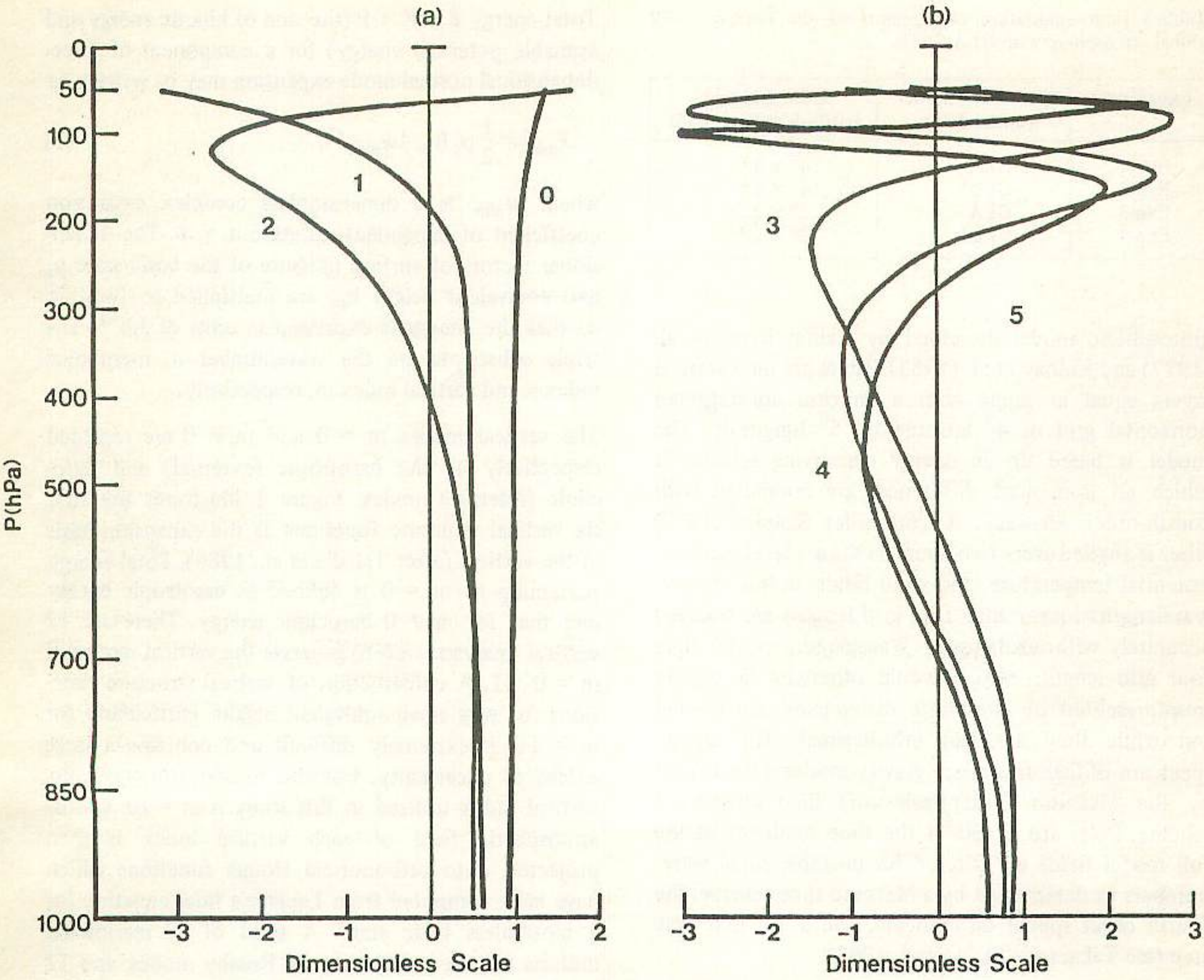

Figure 1 The first six vertical structure functions for the vertical indicies m = 0–5 (after Tanaka et al., 1986).

sums of B_{nlm} and C_{nlm} are zero because they represent the global integral of the flux covergence of kinetic energy and available potential energy. The nonlinear interaction of kinetic energy B is equivalent to a sum of wave-mean and wave-wave interactions of kinetic energy in the standard spectral energetics, and so is the nonlinear interaction of available energy C (see Saltzman, 1957; Kung and Tanaka, 1983). Surface wind at $p = p_s$ has been assumed to vanish as set in Tanaka and Kung (1988).

Using the method of normal mode expansion, we can assess the forecast error in the simulated atmosphere by an error norm between the spectral expansion coefficients of observation w_{nlm} and simulation $\hat{w}_{nlm}$, where the hat designates variables for simulations. A similar evaluation of forecast error is seen using the error norm of spherical harmonic expansions coefficients at a certain vertical level (e.g., Boer, 1984). The present error analysis is based on the information of whole atmospheric field. According to the definition of energy in (1), the error variance ERR in the simulation (actually the apparent error because the observed variables will involve observational errors) may be given as a sum of the following quantities of the normal mode expansion:

$$\mathrm{ERR}_{nlm} = \frac{1}{2} p_s h_m |\hat{w}_{nlm} - w_{nlm}|^2. \qquad (3)$$

The same dimensional factor with (1) is used so that the error variance has physical units of Jm^{-2}. It should be remarked that errors in amplitude and in phase are mixed together in this expression. By means of the inverse of the vertical and Fourier-Hough transforms, it may be shown that the sum of ERR_{nlm} has the same form as total energy $E = K + P$, in which the dependent variables u, v, and ϕ have been replaced by $\hat{u} - u$, $\hat{v} - v$, and $\hat{\phi} - \phi$.

4 Gross Energy Budget for Simulations

One-month average energy spectra and energy interactions are examined in this section. The spectral distributions of total energy E (n) for Rossby modes and gravity modes are illustrated in Figure 2 as functions of wavenumber n for the four simulations. The results of the four simulation experiments, Exp-1 through Exp-4, are distinguished in the figure by a combination of the dashed line (4° × 5° coarse resolution model), solid line (2° × 2.5° fine resolution model), black dot (GLA initial condition), and white circle (GFDL initial condition). The difference of energy spectra at higher wavenumbers between the coarse and fine resolution models is apparent. Both the Rossby modes and gravity modes indicate lower energy levels in the fine resolution models at higher zonal wavenumbers. The gravity modes show a larger reduction than the Rossby modes.

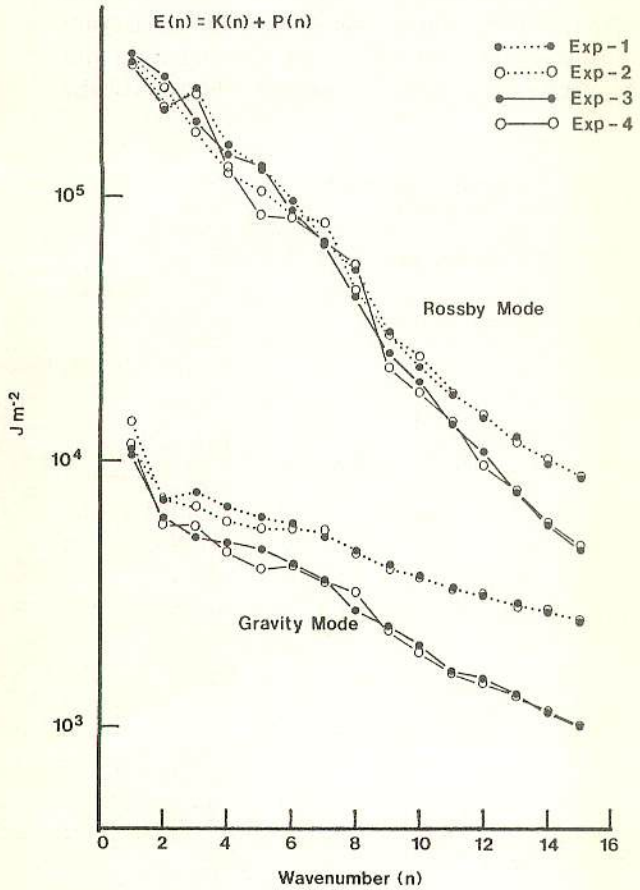

Figure 2 Monthly mean total energy spectra E (n) = K (n) + P (n) of Rossby modes and gravity modes in the zonal wavenumber domain for the four simulations. The simulations are distinguished by coarse (dashed line) and fine (solid line) model resolutions with a combination of GLA (black dot) and GFDL (white dot) initial datasets.

Figure 3 illustrates the total energy spectra E (m) of zonal eddy (n = 1–15) for Rossby modes and gravity modes as functions of vertical indices m. The Rossby modes indicate bimodal energy peaks at the barotropic index m = 0 and baroclinic index m = 3. The bimodal energy peaks were explained by Tanaka and Kung (1989) as the characteristics of atmospheric baroclinic instability for a January basic flow. The gravity modes show the largest energy levels at m = 2–3. Different energy levels between the coarse and fine resolution models at the higher vertical indices of gravity modes are apparent. The increase of horizontal resolution results in a reduction of gravity mode energy levels in the higher order vertical indices. Rossby modes have the same tendency of diminishing energy levels for the higher vertical indices. Vertical energy spectra are not influenced by the different initial conditions provided by the GLA and the GFDL.

It is well-known that the effect of an increased horizontal model resolution appears as an improved eddy energy spectrum. Manabe et al. (1970) found that the increase in the horizontal model resolution improves the general magnitude and the spectral distribution of eddy kinetic energy to be closer to those of the observation due not only to the increase in the accuracy of the

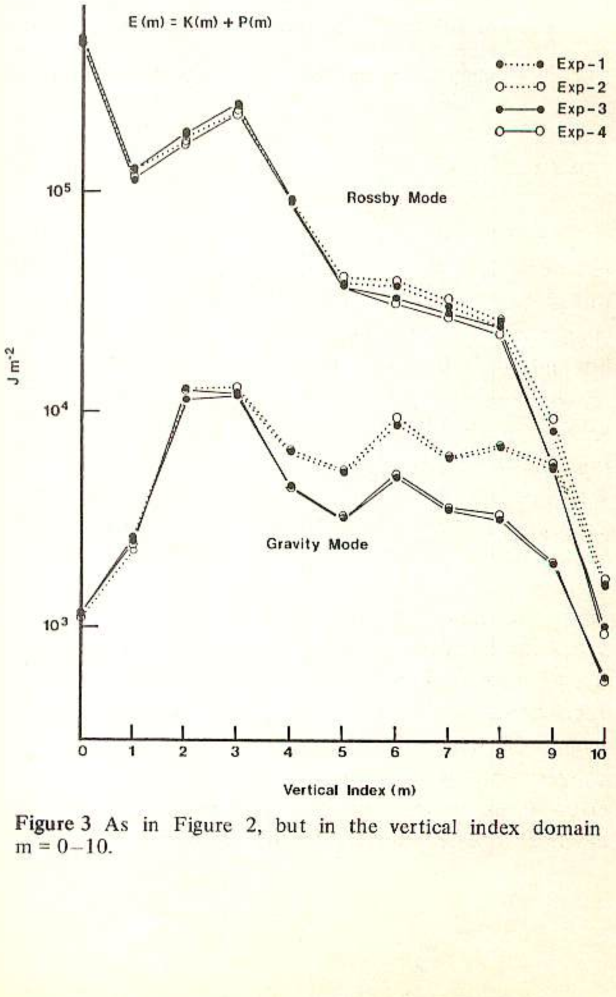

Figure 3 As in Figure 2, but in the vertical index domain m = 0–10.

differences but also to the shift in the scale of dissipation toward smaller scales. Wellck et al. (1971) compared 10°, 5°, and 2.5° mesh model simulations and showed an increase of kinetic energy at the planetary waves in the finer resolution model. Modified up-scale energy cascade from synoptic waves to planetary waves are discussed as the main reason for the improvement. Puri and Bourke (1974) showed an unrealistic accumulation of eddy energy at the shortest resolvable waves in a coarse resolution model. They demonstrated that the accumulation is released in a finer resolution model to reduce the short wave energy. The spectra with the GLA initial conditions and the GFDL initial conditions are indistinguishable. Miyakoda et al. (1986) showed that the circulation patterns of the models tend to be similar to each other on the one-month time scale for three stochastic predictions which start from observed initial conditions derived from three different meteorological centers. The results of their studies agree with the energetics analysis using the normal mode expansion.

The normal mode energetics are summarized in Table 2 in the barotropic (m = 0) and baroclinic (m = 1–10) decomposition of zonal (n = 0) and eddy (n = 1–15) components. The results for the FGGE observations for the winter period from December to February after Tanaka and Kung (1988) are also listed. Compared to the observations, there is a consistent bias of larger zonal barotropic energy in all simulations. Zonal baroclinic energy is closer to the observations. The term B shows large negative values in the eddy baroclinic component (n = 1–15, m = 1–10– and positive values in the eddy barotropic (n = 1–15, m = 0) and zonal barotropic (n = 0, m = 0) components. This indicates kinetic energy transformations from eddy baroclinic to eddy and zonal barotropic components as the net during the period. It is noted that this kinetic energy interaction is significantly larger in simulations than in the observation corresponding to the larger available potential energy interaction C from the zonal baroclinic (n = 0, m = 1–10) to eddy baroclinic n = 1–15, m = 1–10) components. The model biases of large energy level in the zonal field and intense energy transformations were documented in Kung and Baker (1986a) and Tanaka et al. (1986). These deficiencies of the model are not improved by the increase of horizontal resolution and the use of different initial datasets. Kinetic energy supply into the zonal barotropic component (m = 0, n = 0) rather increases with the increase of horizontal resolution. The net diabatic

Table 2 Monthly mean normal mode energy budget for the four simulations. Energy (K, P, and E) in units of 10^5 Jm^{-2} and energy transformations (B, C, D, and dE/dt) in Wm^{-2} are listed for the zonal (n = 0) and eddy (n = 1–15) components in the barotropic (m = 0) and baroclinic (m = 1–10) decomposition. The same energy variables for the FGGE observations during three winter months are after Tanaka and Kung (1988)

n	m	K	P	E	B	C	D	dE/dt
Exp-1								
0	0	9.5	2.9	12.4	0.49	−0.26	0.00	0.23
0	1–10	4.2	46.7	50.9	−0.03	−2.37	2.42	0.02
1–15	0	5.0	0.3	5.3	0.41	0.16	−0.51	0.06
1–15	1–10	4.9	3.8	8.7	−1.72	2.30	−0.54	0.04
Exp-2								
0	0	8.6	2.6	11.2	0.46	−0.25	−0.07	0.14
0	1–10	3.6	42.8	46.3	0.00	−2.30	2.66	0.35
1–15	0	4.3	0.2	4.5	0.39	0.15	−0.49	0.04
1–15	1–10	4.9	3.8	8.7	−1.68	2.34	−0.52	0.13
Exp-3								
0	0	8.7	2.6	11.3	0.64	−0.28	−0.22	0.14
0	1–10	3.7	44.4	48.2	0.13	−2.52	2.59	0.20
1–15	0	4.9	0.3	5.1	0.51	0.17	−0.65	0.03
1–15	1–10	4.7	3.8	8.4	−1.43	2.42	−0.95	0.04
Exp-4								
0	0	9.0	2.7	11.7	0.73	−0.29	−0.23	0.20
0	1–10	3.7	43.3	47.0	0.15	−2.46	2.69	0.37
1–15	0	4.4	0.3	4.7	0.45	0.19	−0.58	0.06
1–15	1–10	4.3	3.5	7.8	−1.47	2.51	−0.98	0.06
FGGE								
0	0	6.5	1.9	8.4	0.47	−0.20	−0.27	0.00
0	1–10	4.1	44.2	48.3	−0.06	−1.85	1.97	0.06
1–15	0	3.6	0.2	3.8	0.33	0.10	−0.44	0.00
1–15	1–10	4.3	3.3	7.6	−0.82	1.63	−0.86	−0.04

process D of the zonal baroclinic component (n = 0, m = 1–10) is larger in the simulations than in the observations. It is also noted that the net diabatic sink D of the eddy baroclinic components (n = 1–15, m = 1–10) is larger in the fine resolution model than in the coarse resolution model.

5 Error Analysis

Error analysis can be used to measure the difference of a model property and that of the forecast skill for different simulations. In the normal mode energetics scheme, the prediction errors are evaluated using the global integrations of the atmospheric fields. We use

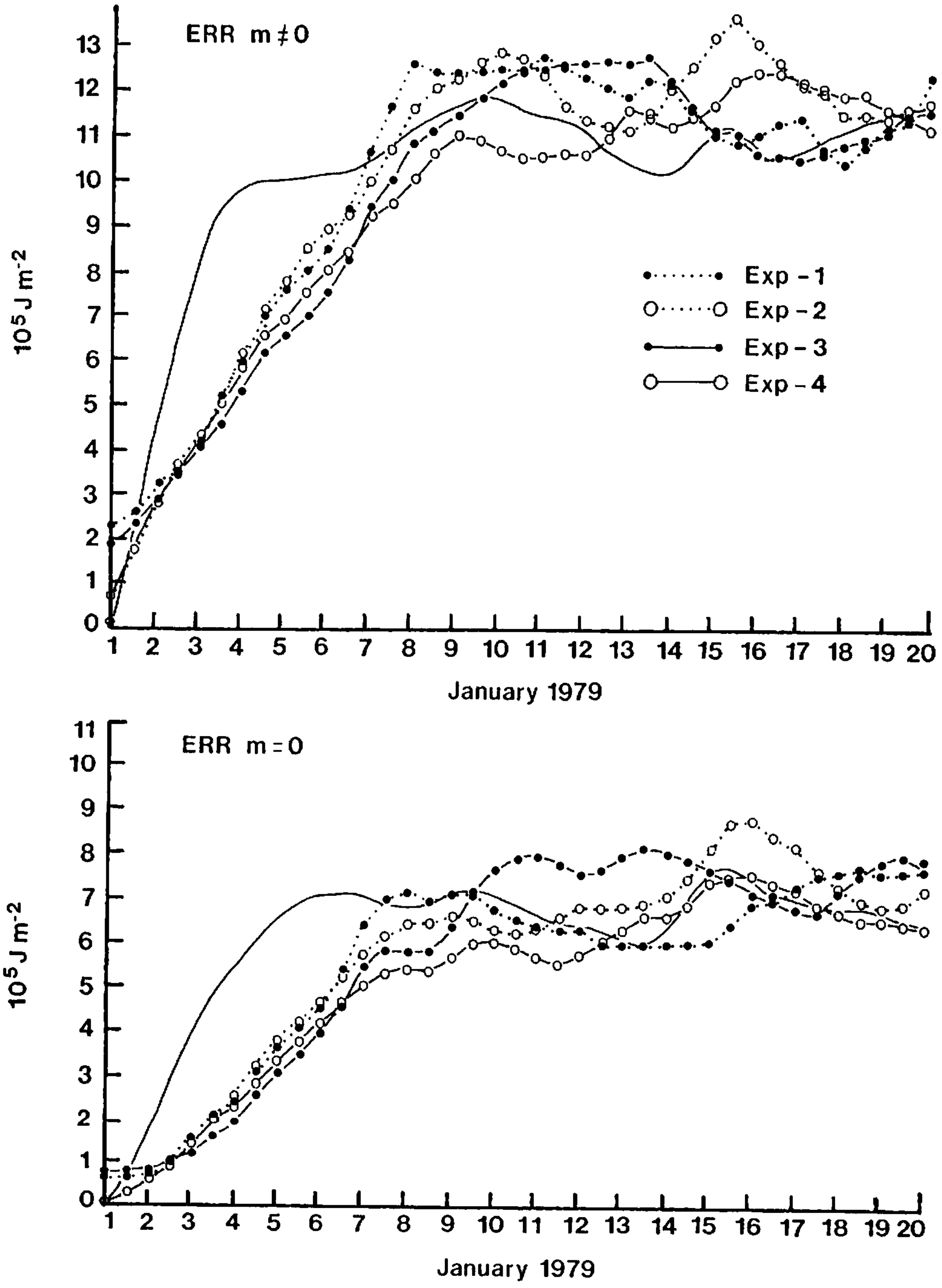

Figure 4 Growth of prediction errors in the four simulations: ERR$_{m\neq0}$ is eddy baroclinic (n = 1–15, m = 1–10) components, and ERR$_{m=0}$ eddy barotropic (n = 1–15, m = 0) components. The simulations are distinguished by coarse (dashed line) and fine (solid line) model resolutions with a combination of GLA (black dot) and GFDL (white dot) initial datasets. Persistence errors starting from 1 January 1979 are presented by a solid line without symbols.

the GFDL analysis of the FGGE data to represent the observed real atmosphere for evaluating the prediction error in model simulations. Although there are other versions of the FGGE analysis, the use of other analysis data should not alter our major conclusions.

Figure 4 illustrates the error growth in eddy field (n = 1–15) of the simulations starting from the initial data of 0000 GMT 1 January. For comparison, the persistence error is presented starting from the same date. The persistence error reaches its saturation level on day 4 in the baroclinic component (m = 1–10), and on day 6 in the barotropic component (m = 0). In contrast, the error energies of the simulations reach their saturation levels around days 8 to 10 in both the barotropic (m = 0) and baroclinic (m ≠ 0) components. Dalcher and Kalnay (1987) proposed the theoretical limit of dynamical predictability as a function of two-dimensional total wavenumber based on the time at which the error energy reaches 95 % of the saturated value. The error growth in the eddy field is slightly reduced in the high resolution model (solid line) compared to the coarse resolution model (doted line). The error energy for the GLA initial data (black dot) on day 1 is about 2 for the baroclinic components and 1 for the barotropic components with units of 10^5 Jm^{-2} because of the different initialization techniques by the GLA and the GFDL. Supposing that these are the estimates of unavoidable initial error, these initial errors acount for more than 10 % of the saturation error energy.

According to Dalcher and Kalnay's (1987) criterion of the dynamical predictability, the error energy of the GLA model reaches 95 % of the saturated value on about day 7. The error energy spectra in the wavenumber domain on day 7 are illustrated in Figure 5 for the barotropic and baroclinic components. The errors are the largest in the planetary waves for n = 1–2 in the baroclinic components, and in the synoptic waves of n = 4–5 for the barotropic components. In interpreting the error energy spectrum, the work of Lorenz (1982) indicates that nonlinear interactions in the system are very effective in amplifying the prediction error and thereby degrading predictability. Yee and Shapiro (1981) and Straus (1988) suggested that the physical instability should play a key role in the growth of mid-latitude forecast error. Straus showed that the synoptic scale (i.e., n = 4–5) peak in the error energy spectrum is due to baroclinic instability, whereas the planetary wave peak is due entirely to nonlinear interactions which transfer error energy from the synoptic scale to the planetary scale. The distinct error energy spectra in the barotropic and baroclinic components in this study may be related partly to the dynamics of the unstable system combined with the nonlinear interaction. However, the separation of these two factors would be difficult. There is a clear difference in the error energy levels between the coarse and fine resolution models. Errors are significantly reduced by the increase of horizontal resolution in the planetary waves (n = 1 and 2) for the barotropic components and in synoptic waves (n = 5) for the baroclinic components.

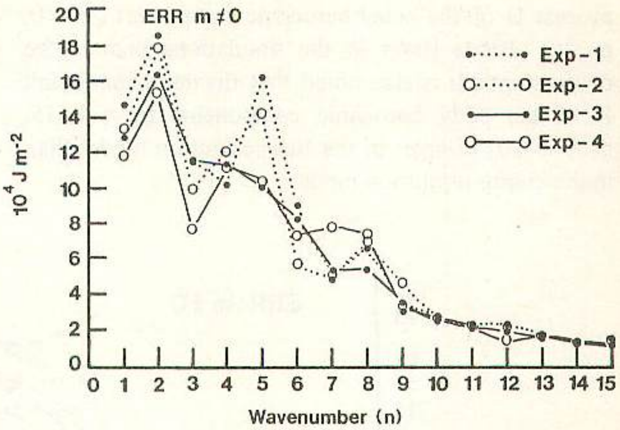

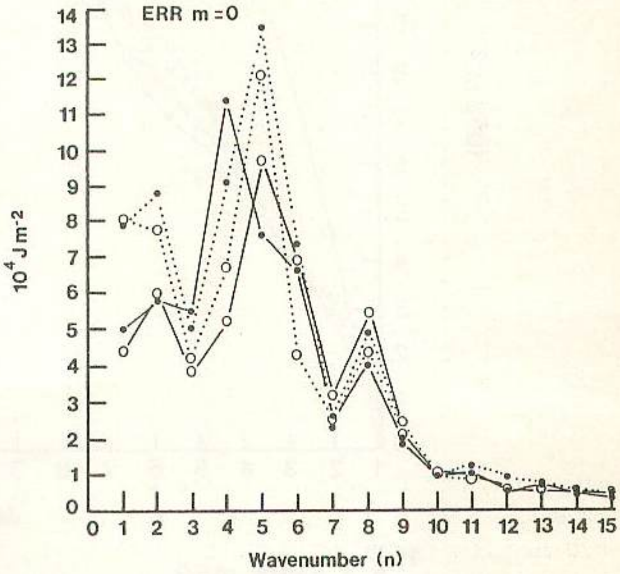

Figure 5 Error energy spectra of the four simulations on date 7: $\mathrm{ERR}_{m \neq 0}$ is baroclinic (m = 1–10) components, and $\mathrm{ERR}_{m=0}$ barotropic (m = 0) components.

Table 3 lists the error energy spectrum in the vertical index domain over n = 0–5 for zonal wavenumbers n = 1–6 and for the sum of eddies n = 1–15 at day 7. The vertical error energy spectra for eddies n = 1–15 show the largest values for the barotropic components (m = 0) and the next largest in the baroclinic component (m = 3). The magnitude of the error energy spectrum appears to be proportional to that of the

Table 3 The error energy spectrum at day 7 in the vertical index domain m = 0–5 for wavenumbers n = 1–6 and the sum of the eddies n = 1–15 in units of 10^5 Jm^{-2}

m	n = 1	n = 2	n = 3	n = 4	n = 5	n = 6	n = 1–15
Exp-1							
0	0.79	0.88	0.50	0.91	1.35	0.74	6.54
1	0.34	0.22	0.22	0.13	0.18	0.07	1.49
2	0.22	0.31	0.30	0.13	0.31	0.17	1.81
3	0.31	0.64	0.34	0.35	0.62	0.33	3.29
4	0.22	0.35	0.17	0.16	0.23	0.14	1.60
5	0.11	0.14	0.07	0.07	0.08	0.05	0.72
Exp-2							
0	0.81	0.77	0.42	0.67	1.21	0.43	5.70
1	0.23	0.20	0.15	0.13	0.14	0.05	1.21
2	0.20	0.33	0.18	0.22	0.34	0.10	1.84
3	0.36	0.56	0.29	0.38	0.52	0.17	2.98
4	0.22	0.33	0.13	0.18	0.16	0.08	1.41
5	0.10	0.16	0.06	0.10	0.06	0.04	0.72
Exp-3							
0	0.50	0.58	0.55	1.14	0.76	0.66	5.48
1	0.32	0.22	0.23	0.14	0.15	0.04	1.35
2	0.23	0.24	0.17	0.22	0.21	0.18	1.76
3	0.25	0.57	0.41	0.39	0.35	0.31	2.96
4	0.17	0.31	0.18	0.18	0.14	0.12	1.38
5	0.09	0.12	0.05	0.08	0.05	0.05	0.61
Exp-4							
0	0.44	0.60	0.38	0.52	0.97	0.69	5.04
1	0.31	0.21	0.12	0.12	0.14	0.10	1.30
2	0.18	0.27	0.13	0.22	0.20	0.14	1.66
3	0.28	0.52	0.24	0.35	0.38	0.25	2.86
4	0.18	0.28	0.09	0.17	0.12	0.10	1.29
5	0.07	0.11	0.04	0.08	0.04	0.04	0.58

energy spectrum in the vertical index domain (see Figure 3). If the vertical spectrum in Figure 3 is a reflection of dominant baroclinic instability as mentioned before, the results suggest a possible connection between the error growth and the instability of the dynamical system, as discussed by Straus. We note that a finite amplitude initial error grows as fast as the fastest growing mode of the unstable dynamical system if the system is linear, although this is not the case in the real atmosphere. It is interesting to note that both baroclinic instability and error growth for numerical weather prediction have a comparable e-folding time of about 2 days. The bimodal error energy peaks are confirmed for all individual zonal waves n = 2–4 in Table 3, except for n = 1. The first internal mode of m = 1 at n = 1 indicates larger error energy compared with that for m = 3, except for the Exp-2. The very large error energy for m = 1 at n = 1 apparently is different from other zonal waves, and will be examined.

6 Vertical Propagation of Wavenumber 1

The unrealistic behavior of the first internal mode m = 1 of wavenumber n = 1 in the GLA simulations has been pointed out by Tanaka et al. (1986). According to our previous result, the simulated component of m = 1 at n = 1, starting from an initial data at 16 December 1978, indicated the minimum amplitude throughout the period without being amplified, while the observed component underwent occasional amplifications corresponding to the vertical propagation of n = 1. Figure 6 shows the time series of total energy E = K + P of the component (n = 1, m = 1) for the observations and simulations starting from the initial data of 1 January 1979. During the integration period, the observed energy is maintained at approximately the same level. In contrast, in all simulations the energy tends to increase during the earlier half of the period. This is a remarkable difference caused by the different initial data compared to our previous experiment. As shown in Table 3, the largest portion of the forecast error for n = 1 in the baroclinic component comes from m = 1. It is noted that m = 1 has an increasingly large amplitude near the top of the model (see Figure 1). This implies that the systematic bias of simulations occurs at the top of the model atmosphere. Figure 6 also demonstrates that there is no improvement by the increase of the model resolution and the use of different initial datasets of 1 January 1979.

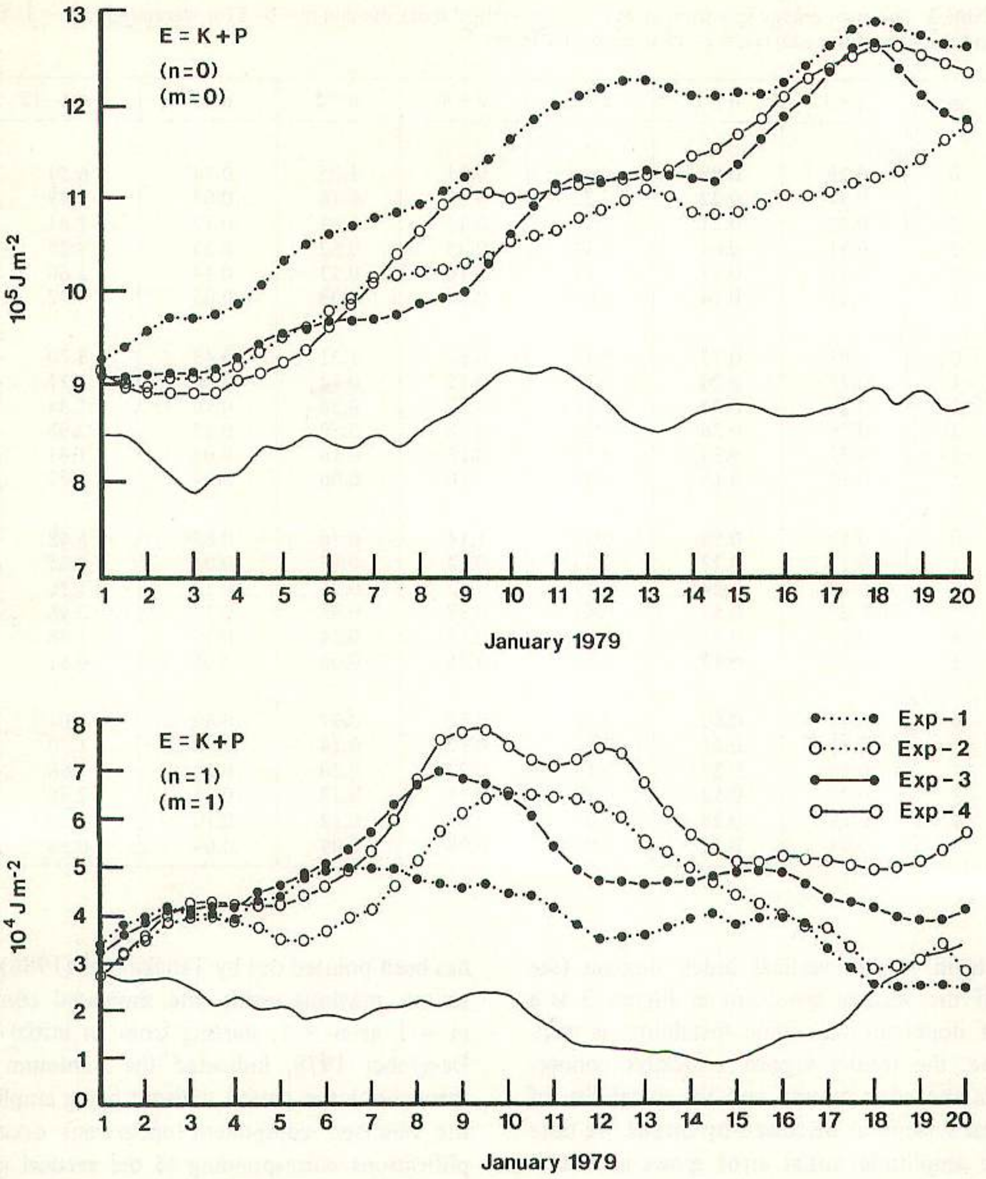

Figure 6 Time series of total energy E = K + P for the first internal modes of wavenumber 1 (n = 1, m = 1). Observed time series of the same component is by a solid line without symbols.

The discrepancy in n = 1 between the simulations and the observations can be traced to the misleading geopotential field near the top of the model atmosphere. Figure 7 shows the observed 5-day means of geopotential height amplitude of n = 1 and 2 in the Northern Hemisphere during 7–11 January 1979. The same meridional-height cross sections in the simulations for n = 1 are shown in Figure 8. Geopotential height in these figures is multiplied by a common dimensionless factor of $(p/p_s)^{1/2}$ in order to remove the basic density stratification effect. In Figures 7 and 8 the discrepancies in geopotential height fields in the simulations are evident. During days 7–11 a large-scale Pacific blocking with a high-low vortex pair reaches its mature stage (Kung and Baker, 1986b). Related to this Pacific blocking, a clear dipole structure of n = 1 appears in the meridional cross section of Figure 7 indicating two amplitude maxima at 45 °N and 75 °N. The northern pole has its height ridge over Alaska, and the southern pole has its trough over the Pacific Ocean. The amplitude peaks appear at 500 mb. Such a clear dipole structure is not observed for n = 2. The basic structure of this Pacific blocking can be described by superimposing the dipole structure of n = 1 on that of n = 2. On the other hand, in simulations, the dipole structure of n = 1 is not well handled.

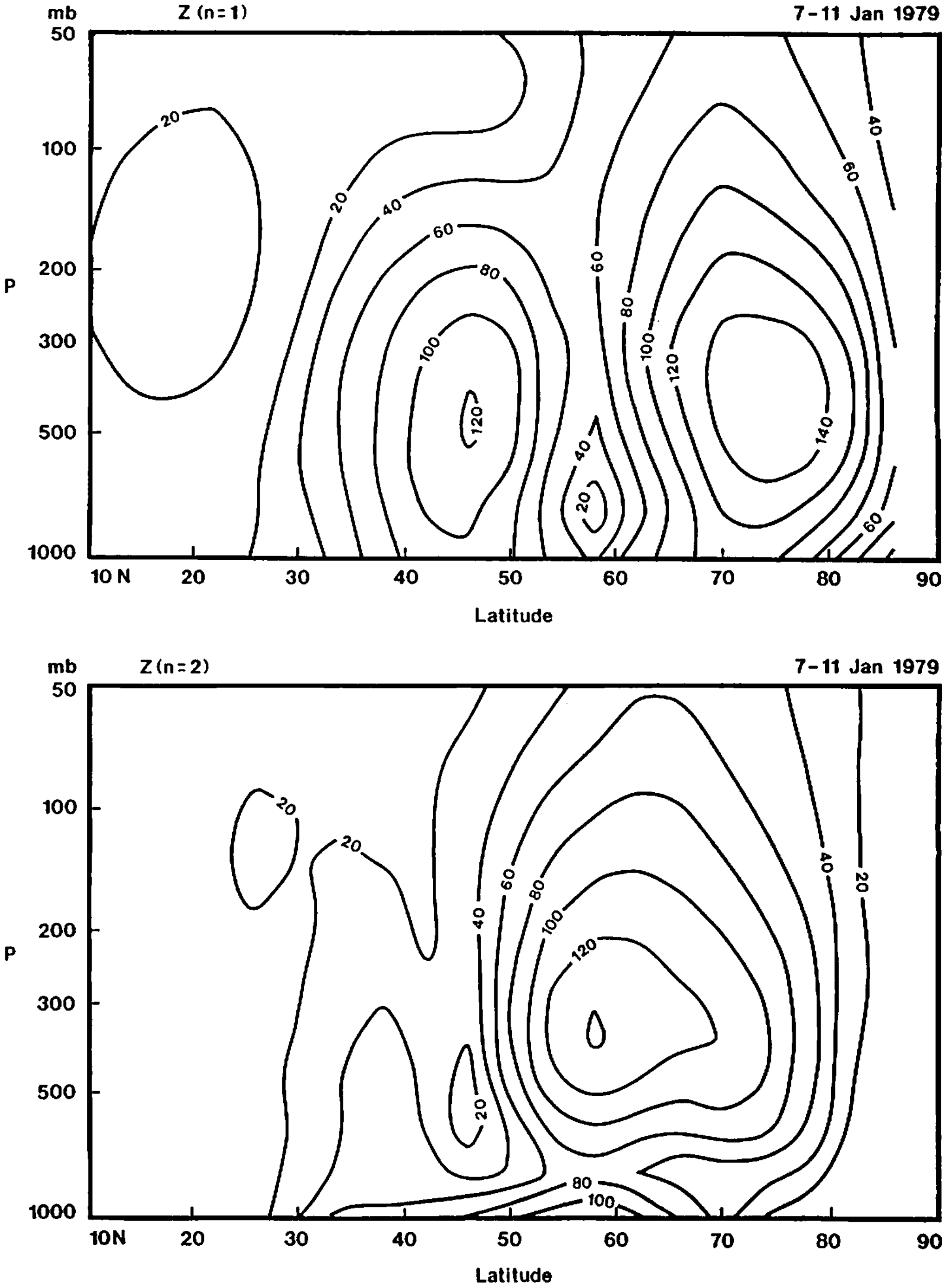

Figure 7 Meridional-height cross sections of geopotential height amplitude Z in the Northern Hemisphere for wavenumbers n = 1 and 2. The values are observed 5-day means for 7–11 January 1979, and are weighted by $(p/p_s)^{1/2}$ to remove the density stratification effect.

The northern part of the amplitude maximum propagates away into the stratosphere. This discrepancy of unrealistic vertical propagation in simulations may explain the systematic bias in the energy of the increasing first internal vertical mode of n = 1 as shown in Figure 6.

7 Concluding Summary

Comparative energetics are presented for four one-month GLA GCM simulations for January 1979, integrated from initial conditions at 0000 GMT 1 January 1979. These four numerical experiments involve a combination of two different horizontal

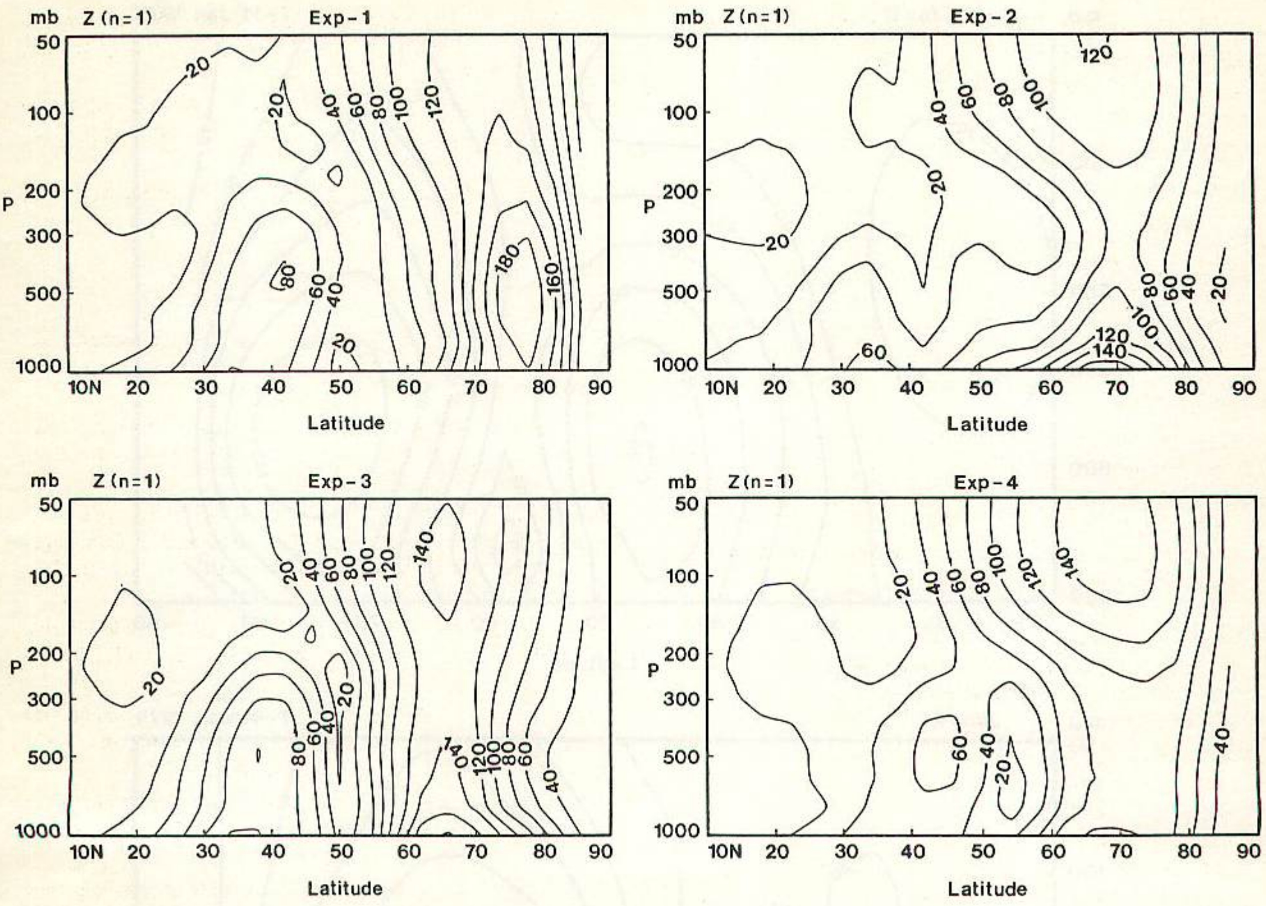

Figure 8 As in Figure 7, but for the four simulations during the same period.

grid resolutions and two sets of initial conditions prepared by the GLA and GFDL. The effect of increased horizontal resolution from the standard 4° x 5° latitude-longitude grid to the 2° x 2.5° grid, and the effect of the initial datasets upon the climatic drift of the model are examined using a recently developed normal mode energetics scheme.

For one-month averages of the time integrations, it is found that the gravity mode energy levels are significantly reduced in the higher wavenumbers and in the higher order internal vertical modes by the increase in horizontal model resolution. The strong zonal jet with the barotropic structure, and the intense wave-mean interaction of kinetic energy from eddy to zonal field in the simulations, as documented by Tanaka et al. (1986) and Kung and Baker (1986a), are not improved by the increase of model resolutions or different initial conditions.

In the method of the normal mode expansion the prediction errors of the model experiments may be measured by the error norm between the two spectral expansion coefficients of observed and simulated atmosphere. It is found that the increase of the model resolution reduces the prediction error in planetary waves for n = 1 and 2 of the barotropic component and in synoptic waves for n = 5 of the baroclinic component. It is also apparent that the misleading vertical propagation of planetary waves into the model stratosphere results in a common bias of the prediction in the first internal vertical component (m = 1) of wavenumber 1. This bias is related to a misrepresentation of the Pacific blocking occurring at the predictability limit of the model atmosphere.

Acknowledgements

The authors gratefully acknowledge the courtesy of Drs. K. Miyakoda and J. J. Ploshay of the Geophysical Fluid Dynamics Laboratory in providing the GFDL initial data, and the assistance of Y. Brin and L. Takacs in the numerical experiments at the Goddard Space Flight Center. The authors are also thankful to S. Humphrey, V. Peters, G. Vickers and D. K. Williams for their Technical Assistance. This research was performed at Eck Research Consulting Inc. under the National Aeronautics and Space Administration Contract NAS5-30128.

References

Boer, G. J., 1984: A spectral analysis of predictability and error in an operational forecast system. Mon. Wea. Rev., **112**, 1183–1197.

Charney, J. G., R. G. Fleagle, V. W. Lalley, H. Riehl and *D. Q. Wark,* 1966: The feasibility of a global observational and analysis experiment. Bull. Amer. Meteor. Soc., 47, 200–220.

Dalcher, A. and *U. Kalnay,* 1987: Error growth and predictability in operational ECMWF forecast. Tellus, **39A**, 474–491.

Daley, R., A. Hollingsworth, J. Ploshay, K. Miyakoda, W. Baker, E. Kalnay, D. Dey, T Krishnamurti and *E. Baker,* 1985: Objective analysis and assimilation techniques used for the production of FGGE IIIb analyses. Bull. Amer. Meteor. Soc., 77, 532–540.

Kalnay, E., R. Balgovind, W. Chao, D. Edelmann, J. Phaendtner, L. Takacs and *K. Takano,* 1983: Documentation of the GLAS fourth order general circulation model. NASA Tech. Memo, **86064**, (NTIS N8424028).

Kalnay-Rivas, E., A Bayliss and *J. Storch,* 1977: The fourth order GISS model of the global atmosphere. Beitr. Phys. Atmosph., **50**, 299–311.

Kung, E. C. and *W. E. Baker,* 1986a: Comparative energetics of the observed and simulated global circulation during the special observing periods of FGGE. Quart. J. R. Met. Soc., **112**, 593–611.

Kung, E. C. and *W. E. Baker,* 1986b: Spectral energetics of the observed and simulated Northern Hemisphere general circulation during blocking episodes. J. Atmosph. Sci., **43**, 2792–2812.

Kung, E. C. and *H. Tanaka,* 1983: Energetics analysis of the global circulation during the special observation period of FGGE. J. Atmos. Sci., **40**, 2575–2592.

Lorenz, E. N., 1982: Atmopsheric predictability experiments with a large numerical model. Tellus, **34**, 505–513.

Manabe, S., J. Smagorinsky, J. L. Holloway, Jr. and *H. M. Stone,* 1970: Simulated climatology of a general circulation model with a hydrologic cycle. Mon. Wea. Rev., **98**, 175–213.

Miyakoda, K., R. F. Strickler, C. J. Nappo, P. L. Baker and *G. D. Hembree,* 1971: The effect of horizontal grid resolution in an atmospheric circulation model. J. Atmos. Sci., **28**, 481–499.

Miyakoda, K., J. Sirrutis and *J. Ploshay,* 1986: One-month forecast experiments without anomaly boundary forcing. Mon. Wea. Rev., **114**, 2363–2401.

Puri, K. and *W. Bourke,* 1974: Implications of horizontal resolution in spectral model integrations. Mon Wea. Rev., **102**, 333–347.

Salztman, B., 1957: Equations governing the energetics of the larger scales of atmospheric turbulence in the domain of wave number. J. Meteor., **14**, 513–523.

Shapiro, R., 1970: Smoothing, filtering, and boundary effects. Rev. Geophys. Space Phys., **8**, 359–387.

Shukla, J., 1985: Predictability. Issues in Atmospheric and Oceanic Modeling. Advance in Geophysics, **28**, (ed., S. Manabe) Academic Press, 87–122.

Smagorinsky, J., 1969: Problems and promises of deterministic extended range forecasting. Bull. Amer. Meteor. Soc., **50**, 286–311.

Straus, D. M., 1988: The dynamics of error growth in a quasi-geostrophic channel model. Proc. The Eighth Conference on Numerical Weather Prediction, Americ. Meteor. Soc., 614–616.

Takacs, L. L. and *R. C. Balgoving,* 1983: High-latitude filtering in global grid-point models. Mon. Wea. Rev., **111**, 2005–2015.

Tanaka, H., 1985: Global energetics analysis by expansion into three-dimensional normal mode functions during the FGGE winter. J. Meteor. Soc. Japan, **63**, 180–200.

Tanaka, H. L. and *E. C. Kung,* 1988: Normal mode energetics of the general circulation during the FGGE year. J. Atmos. Sci., **45**, 3723–3736.

Tanaka, H. L. and *E. C. Kung,* 1989: A study of low-frequency unstable planetary waves in realistic zonal and zonally varying basic states. Tellus, **41**, (in press).

Tanaka, H., E. C. Kung and *W. E. Baker,* 1986: Energetics analysis of the observed and simulated general circulation using three-dimensional normal mode expansions. Tellus, **38A**, 412–428.

Wellck, R. E., A. Kasahara, W. M. Washington and *G. D. Santo,* 1971: Effect of horizontal resolution in a finite-difference model of the general circulation. Mon. Wea. Rev., **99**, 673–683.

Williamson, D. L. and *A. Kasahara,* 1971: Adaption of meteorological variables forces by updating. J. Atmos. Sci., **28**, 113–1324.

Yee, S. Y. K. and *P. Shapiro,* 1981: The interaction of model dynamics and numerical errors in a nondivergent global barotropic model. Mon. Wea. Rev., **109**, 687–700.

Article

Beitr. Phys. Atmosph., June 1989, p. 112–125
0005–8173/89/02 0112–14 $ 3.00/0

Vol. 62, No. 2

On the Structure of the Global Linearized Primitive Equations
Part II: Laplace's Tidal Equations

R. Müller

Max-Planck-Institut für Chemie, Postfach 3060, D-6500 Mainz, FRG

(Manuscript received in May 1988; revised form accepted February 1989)

Abstract

Eigenfunctions and eigenfrequencies of Laplace's tidal equations have been computed for both negative and positive values of the Lamb parameter $\epsilon = 4\Omega^2 a^2/(gD)$. Positive values of ϵ correspond to stable conditions. In this case real eigenfrequencies that can be associated with three types of atmospheric waves occur, namely: Rossby waves, eastward and westward travelling gravity waves. Negative ϵ, i.e. negative equivalent depth D, corresponds to unstable conditions, and thus some of the eigenvalues are found to be complex in this case. These eigenfrequencies appear in complex conjugated pairs for the gravity-type modes. All the modes associated with Rossby waves remain real. As a crude parametrization of dissipation mechanisms Rayleigh friction is included in the model. This leads also to imaginary parts of the eigenfrequencies. Various asymptotic forms of the solutions are discussed.

Zusammenfassung

Über die Struktur der globalen linearisierten primitiven Gleichungen
Teil II: Die Laplaceschen Gezeitengleichungen

Eigenfunktionen und Eigenfrequenzen der Laplaceschen Gezeitengleichungen werden für negative und positive Werte des Lamb-Parameters $\epsilon = 4\Omega^2 a^2/(gD)$ berechnet. Positive Werte von ϵ entsprechen stabilen Verhältnissen. In diesem Fall treten ausschließlich reelle Eigenfrequenzen auf, die drei Typen atmosphärischer Wellen zugeordnet werden können: Rossby-Wellen sowie ost- und westwärts laufenden Schwerewellen. Negatives ϵ, also negative ‚equivalent depth' D entspricht instabilen Verhältnissen, demzufolge Schwerewellen teilweise komplexe Eigenfrequenzen (in komplex konjugierten Paaren) besitzen. Alle Moden, die Rossby-Wellen zugeordnet werden, bleiben reell.

Zur Berücksichtigung dissipativer Reibungseffekte wird ein einfacher Ansatz vom Rayleigh-Typ verwendet. Er verursacht in den Eigenfrequenzen ebenfalls Imaginäranteile. Verschiedene asymptotische Formen der Lösungen werden diskutiert.

1 Introduction

The shallow water equations on a rotating sphere are of fundamental interest for the theory of both the atmosphere and ocean. If they are formulated in linearized form (with respect to a basic state at rest) for an incompressible, homogeneous and hydrostatic fluid they are called Laplace's tidal equations. They may alternatively be derived through the separation of a primitive equation model that describes a similar problem but with the inclusion of compressibility and stratification (e.g. Müller, 1989; hereafter referred to as part I). The first to obtain solutions for Laplace's tidal equations at least for asymptotic cases was Margules (1893). Independently, Hough (1898) found similar solutions by employing a spherical harmonic expansion, which became the standard technique later. The eigenfunctions of Laplace's tidal equations are therefore called Hough functions (Siebert, 1961). A thorough study of Laplace's tidal equations has been performed by Longuet-Higgins (1968), who calculated stable solutions for positive and negative values of the Lamb parameter ϵ and for zonal wavenumber $m = 0–5$. Kasahara (1976) presented a similar, somewhat more concise treatment, and Swarztrauber and Kasahara (1985) have shown that a compact and lucid approach is possible using spherical vector harmonics. The work of Longuet-Higgins was extended for negative Lamb parameter ϵ by Jones (1972), who calculated unstable solutions, and Volland (1974) who included complex frequencies to model dissipation.

In this study we will follow the approach of Swarztrauber and Kasahara (1985) but will also include Rayleigh friction and consider negative values of ϵ with the corresponding unstable solutions.